AIP Review of Scientific Instruments

Versatile optical access to the tunnel gap in a low-temperature scanning tunneling microscope

K. Kuhnke, A. Kabakchiev, W. Stiepany, F. Zinser, R. Vogelgesang et al.

Citation: Rev. Sci. Instrum. **81**, 113102 (2010); doi: 10.1063/1.3480548
View online: http://dx.doi.org/10.1063/1.3480548
View Table of Contents: http://rsi.aip.org/resource/1/RSINAK/v81/i11
Published by the American Institute of Physics.

Versatile optical access to the tunnel gap in a low-temperature scanning tunneling microscope

K. Kuhnke,[1] A. Kabakchiev,[1] W. Stiepany,[1] F. Zinser,[1] R. Vogelgesang,[1] and K. Kern[1,2]
[1]*Max-Planck Institute for Solid State Research, Heisenbergstrasse 1, D-70569 Stuttgart, Germany*
[2]*Institut de Physique de la Matière Condensée, Ecole Politechnique Fédérale de Lausanne, CH-1015 Lausanne, Switzerland*

(Received 19 March 2010; accepted 26 July 2010; published online 8 November 2010)

We developed a setup that provides three independent optical access paths to the tunnel junction of an ultrahigh vacuum low temperature (4.2 K) scanning tunneling microscope (STM). Each path can be individually chosen to couple light in or out, or to image the tunnel junction. The design comprises *in situ* adjustable aspheric lenses to allow tip exchange. The heat input into the STM is negligible. We present in detail the beam geometry and the realization of lens adjustment. Measurements demonstrate the characterization of a typical light source exemplified by emission from tip-induced plasmons. We suggest employing the Fourier transforming properties of imaging lenses and polarization analysis to obtain additional information on the light emission process. Performance and future potential of the instrument are discussed. © *2010 American Institute of Physics.* [doi:10.1063/1.3480548]

I. INTRODUCTION

The observation of luminescence stimulated by the localized tunneling current in a scanning tunneling microscope has become a valuable technique for the characterization of tip-induced plasmon emission from metal surfaces[1,2] and luminescence from semiconductor quantum structures[3] or molecules adsorbed on surfaces.[4–6] The combination of light spectroscopy with electronic tunneling spectroscopy can provide deep insight into excitation mechanisms of adsorbed molecules.[7] The experimental technique allows the combination of the high spatial definition of the injected tunneling current (<1 nm) with the virtues of optical spectroscopy. The latter provides a performance which is not achieved by a scanning tunneling microscope (STM) alone: (1) high relative energy resolution ($\lambda/\Delta\lambda>10^3$) using optical spectrometers, (2) characterization of the light emitting process by light polarization analysis,[8] and (3) luminescence time-correlation measurements.[9]

Instrumental designs, which serve the previously discussed or similar types of experiments, have been presented by different groups.[10–15] Our approach to optimize light detection continues these developments and adds several new perspectives. Polarization analysis and time correlations of the emitted light can be fully exploited only if free propagating light beams are used instead of beams guided by optical fibers. In addition, free propagating beams preserve the angular emission distribution of the light source, which we will discuss in detail below. Experiments in UHV at liquid He temperature provide superior stability and reproducibility with respect to STM performance and sample characterization. Low temperature setups have thus been realized earlier, e.g., by separate cooling of an externally adjusted lens to liquid nitrogen temperature,[11,16] collecting by optical fibers,[17] or the use of a conductive transparent tip attached to a fiber.[18] Maintaining the instrument constantly at liquid He temperature while using free propagating beams requires a new design which restricts thermal input into the STM.

The goal of maximized light collection efficiency can be achieved by employing an ellipsoidal[19] or parabolic mirror[10] surrounding the tip-sample region. Such a solution also allows eliminating completely chromatic aberration. Our aim to integrate a highly versatile optical setup into an already operating STM system with the important features of tip and sample exchange, easy optical adjustment, and high mechanical stability leads us to a compromise providing still fairly good collection efficiency and achromaticity.

II. EXPERIMENTAL DETAILS

A. Basic design idea

The setup presented in this paper requires a full (three translational degrees of freedom) *in situ* readjustment of the collecting optics with respect to the STM-tip over a range of at least 0.3 mm (positional variation of different tips) and a precision of adjustment of about 10 μm (a few times the optical resolution). The optics is cooled to the same temperature as the whole STM assembly and heat input is very efficiently suppressed by focusing the light from the tunnel junction through two small holes that serve to confine also the solid angle for radiation input from the room temperature environment.

We chose a geometry [Figs. 1(a) and 1(b)] with three aspheric lenses mounted at azimuths 90° from one another and their optical axis at 30° elevation angle from the sample plane. Each lens has a numerical aperture (NA) of 0.42 yielding a collecting area of 9.2% of the half sphere per lens. The total solid angle of light collected from the tunneling gap is, however, not the most relevant figure because, first, luminescence emission toward the surface normal is not possible due to blocking by the STM tip itself and second, the emission

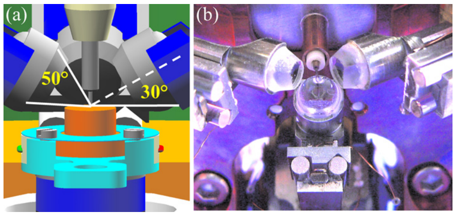

FIG. 1. (Color online) (a) Computer aided design (CAD) image (Ref. 30) of the lens arrangement near the tip-sample tunnel junction. The optical axes form an angle of 30° with respect to the surface plane. The acceptance angle of each lens is 50°. (b) Photograph of the assembly of the tip and the three lenses without a sample.

intensity at grazing angle tends toward zero. More relevant is, in fact, the collection of light around the elevation of maximum emission which is situated approximately 60° off the surface normal.[11] From the light emitted on the 60° cone the three lenses collect 47% of the light. A higher value would be achieved if the lens axes were separated by angles smaller than 90°. However, for a better interpretation of measurements, we decided to provide clearly defined parallel (180°) or orthogonal (90°) observation directions when projected onto the sample surface. Reflection losses at the uncoated surfaces of lenses and viewports can, in total, add up to 20%–25%. We thus estimate total collection efficiencies of 21% and 35% for the two limiting cases of isotropic radiation and radiation exclusively on the 60° cone, respectively. As will be discussed in Sec. III E, the chromatic aberration can lead to additional wavelength-dependent losses for wavelengths for which the focus is not optimized.

We remark that the exchange of tip and sample requires full access from one side so that one quarter of the cone cannot be equipped with a light collection unit. The commercial lenses (for details see Sec. II E) were polished on their sides to obtain a conical shape near the entrance face [see Fig. 1(b)] which avoids mechanical collision between adjacent lenses and collision between lenses and sample surface. In fact, the optical performance is not remarkably impaired by this treatment and the numerical aperture is not reduced.

Figure 2 shows in detail the unit carrying one lens. Each lens is adjustable by ±3 mm along the beam direction for focusing and ±1 mm in the perpendicular (x/y) plane. Adjustment is done by a single four-segment piezotube operated in slip-stick motion (outer diameter of 10 mm, inner diameter of 9 mm, and length of 18 mm; supplier: Physik Instrumente, Germany). The direction of motion is controlled in a standard way by sign and amplitude of saw-tooth pulses applied to the four piezosegments with respect to the grounded inner electrode. The adjustment of the lenses with respect to the tip is thus simple and can be easily monitored by three low-cost digital cameras mounted outside the vacuum chamber at the end of each optical path. The aspherical lenses provide good light collection efficiency over the range of visible wavelengths and a sufficient imaging quality with a wavelength-dependent resolution limit of 2–4 μm. This is an important result as the lens is from the manufacturer's side specified by a design wavelength of 980 nm, which means that the aspheric shape has been optimized for wavelengths, which are longer than typically used in experiments

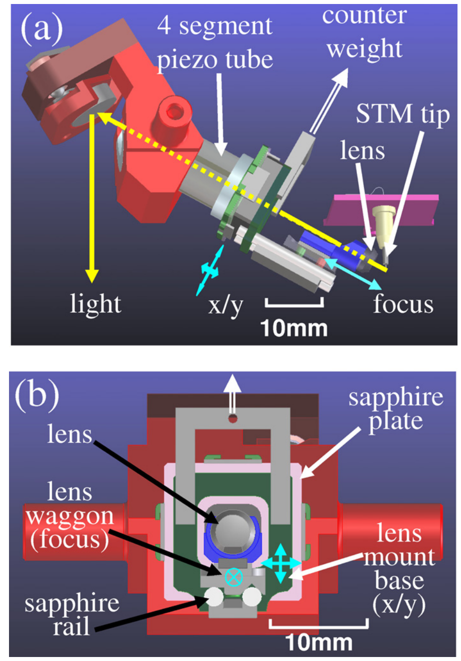

FIG. 2. (Color online) CAD images (Ref. 30) of one of the three lens adjustment units. (a) Side view with tip holder and (b) head-on view in the direction of light propagation. The principal parts are described in the text.

discussed here. The use of lenses (instead of mirrors) provides some chromaticity discussed in the experimental part below. Moreover, glass lens and glass UHV viewports presently restrict the detectable light to the visible and near IR range.

The three lenses couple light from the tunnel junction via three flat mirrors into three vertical light paths with the beams propagating in vacuum [Fig. 3(b)]. After passing through UHV viewports the paths end outside the UHV chamber in three independent ports which can be employed in various combinations. Each port can be equipped with a web camera (for lens adjustment), with an intensified camera, with a spectrometer, or with a single channel light de-

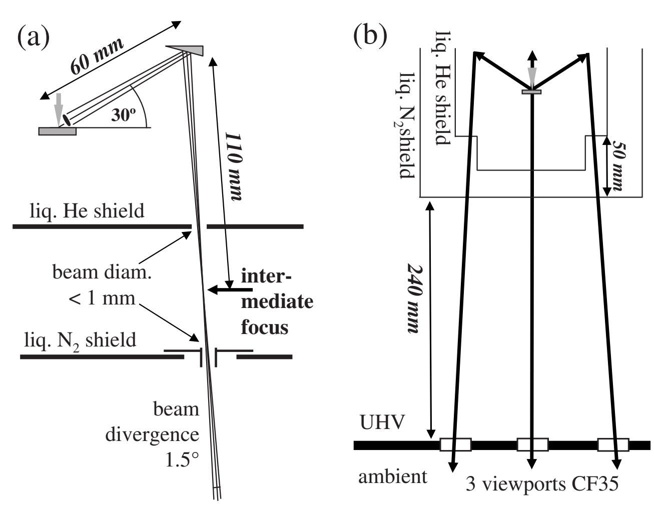

FIG. 3. (a) Beam geometry of one of the three optical paths. For details of the beam passing through the two cryostat shields, see text. (b) Schematic cross section of the STM, the cryostat, and the bottom flange of the UHV chamber. The three beam paths are indicated by lines with arrows.

tector (such as, e.g., a photomultiplier tube or avalanche photodetector). By reversing the propagation direction, light can also be coupled into each port providing directional illumination on the sample, e.g., for photoluminescence experiments.

B. The scanning tunneling microscope

The STM setup comprises an exchangeable plate, which holds the tip (top) and an exchangeable sample mounted in a magnetizable sample holder (bottom). The sample holder is held in position by a magnet glued to an eight-segment scan piezo (supplier: Stavely sensors, Inc., USA). One ring of four segments is employed for horizontal scanning and four segments are interconnected to control the tip-sample distance (vertical offset during scanning). The scanning unit is mounted on a home-built coarse approach motor which allows horizontal and vertical positioning over a range of several millimeters. In this paper, we do not focus on the performance of the setup as a scanning tunneling microscope. For this, the reader is referred to the appropriate literature. With respect to our instrument, we refer to Ref. 20. Most important for the further discussion of the optical setup is the fact that the STM tip is fixed and all the relative motion between tip and sample during coarse approach and during STM scanning is made by the sample. The lens units are attached to the same base as the tip holder so that the relative adjustment of tip and lenses does not change by sample exchange and during STM operation.

C. The light path

The detailed geometry of the light paths is shown in Figs. 1–3. The entrance surface of the aspheric lens is typically adjusted to a distance of 2.5 mm from the tip apex. The lens focuses the light to an intermediate focus 170 mm behind the lens. From the lens the light passes inside the piezotube (inner diameter of 9 mm) and is reflected from an *ex situ* adjusted commercial silver mirror. The light exits the cryogenic part of the setup through holes in the two radiation shields. The intermediate focus is situated between the inner radiation shield at liquid He temperature and the outer shield at liquid nitrogen temperature [Fig. 3(a)]. The focus prevents any blocking of the luminescence light by the holes which act as apertures only when a wider area of the surface is imaged. In the reverse direction, the holes in the two radiation shields (diameter of 4 mm in the liquid He shield and 6 mm in the liquid N_2 shield) reduce the thermal background radiation entering the STM. The negligible heat input into the 4.2 K system is reflected by the fact that the liquid He consumption remained unchanged comparing the situations before and after the holes in the shields were implemented. Calculation of the heat input assuming perfect black body radiation ($\varepsilon=1$) from the 300 K environment through a 28 mm^2 hole at a solid angle 2 msr yields an upper limit of the input power of 5 μW. The direct radiation on each lens (solid angle 0.4 msr) is less than 1 μW. This IR radiation is predominantly absorbed by the lens and only a minor part is transmitted to the tunnel junction.

The STM is firmly mounted on the liquid He tank, which, however, is not rigidly attached to the liquid nitrogen tank so that the relative alignment of the holes in the two radiation shields can change. In order to allow for adjustment, rather large holes were drilled into the liquid nitrogen shield. These holes are each covered by a plate containing a tube with a much smaller inner diameter (6 mm). Moving plate and tube from the outside of the UHV chamber by a wobble stick allows aligning the holes in the liquid nitrogen shield with the fixed holes in the liquid He shield [Fig. 3(a)]. After traversing the UHV viewports vertically [Fig. 3(b)] the light from the tunnel junction is reflected by 90° to horizontal propagation and focused by a lens on the corresponding optical detector or camera.

D. Lens adjustment by slip-stick motion

The *in situ* adjustment of the three lenses is a central point for the operation of the setup. Lenses and motors are mounted on the liquid He tank and thus operated at 4.2 K in UHV. Under the standard focusing conditions described above, a change of tip position by more than 50 μm requires lens readjustment to avoid losses at the holes in the cryogenic shields. *Ex situ* preadjustment of the STM tips on their mounts yields a reproducibility of only $\approx$300 μm. The fact that the exchange of an STM tip always requires a readjustment of the lenses emphasizes the importance of an easy-to-use *in situ* lens adjustment.

Figure 2 shows one lens unit. Focusing of the lens (z-motion) is guided by two sapphire rods which act as rails. The motion is controlled by applying saw-tooth voltage pulses equally to the four piezo segments with respect to the inner grounded contact. Applying saw-tooth pulses with opposite sign to opposite segments leads to lateral (x, y) motion of the entire lens mount including the rails. The x/y plane of motion is defined by a sapphire plate whose surface normal is parallel to the light beam, i.e., tilted by 60° with respect to the direction of gravitation. In order to compensate for the weight in the up/down motion the lens mount base is pulled upwards by a wire which is attached to an appropriate counter weight.

Slip-stick motors require a controlled force normal to the contact surface. As the STM setup does not feature coils for the generation of high magnetic fields, the normal force can be implemented by the magnetic force between permanent magnets and magnetizable steel. In other cases, springs may serve the same purpose although the resulting normal force will change with operation temperature, which might make the operation less reliable.

E. Materials

The lens adjustment unit is composed of different materials that respond to specific requirements. The unit is made from UHV-compatible materials such as tantalum, sapphire, magnetizable and nonmagnetizable steel, Al_2O_3 ceramics, and others. In particular, $Co_{17}Sm_2$ magnets (supplier: Peter Welter GmbH & Co. KG, Germany) were employed to control normal forces in the slip-stick motors. The different parts

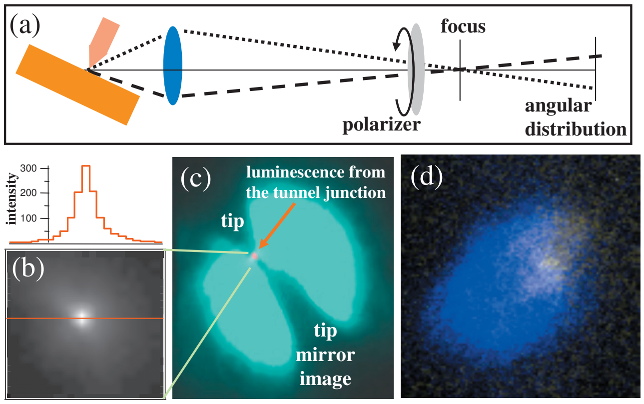

FIG. 4. (Color) (a) Schematic geometry of polarization and angular distribution measurements. Image of the tunnel junction and luminescence light source: (b) focal image (below) and cross section (red line, above) of the intensity distribution of the light emitted by tip-induced plasmons. (c) Overlay of the luminescence focal image (red) with the shadow image of the tip and its mirror image illuminated from the back (cyan). (d) Overlay of the angular distributions of the component polarized along the surface normal (p-polarization, blue) and the perpendicular component (s-polarization, green). The yellow region indicates roughly identical intensities of the two polarizations.

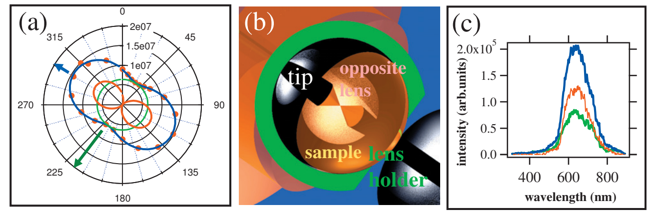

FIG. 5. (Color) (a) Polar plot of the polarization-dependent spectrally integrated intensity for emission from tip-induced plasmons. (b) Simulation of tip-sample geometry for the measurements in (a). (c) Spectra recorded along the two principle axes of linear polarization. The color coding is the same as in the polar plot (a). From a single photon calibration, an estimate of absolute photon numbers is obtained by dividing the arbitrary units by 50.

are glued together by UHV-compatible conductive and nonconductive epoxy glues.

The optical properties of UHV components (e.g., the birefringence of UHV glass viewports) are rarely specified by manufacturers. Similarly, the UHV compatibility of commercial optical components is in general not guaranteed and has to be tested prior to usage. We observed no significant outgassing at 100 °C in vacuum for the aspheric lenses (uncoated precision molded aspheric lens, Corning C0550 glass, Light Path Technologies, Inc., USA, supplier: Edmund Optics) and the plane mirrors (Ag protected coating ER.2, Newport Corp.).

III. EXAMPLES OF LUMINESCENCE CHARACTERIZATION

A. Monitoring the luminescence source

We employ low-cost web cameras to monitor the tip approach. They are, however, not sensitive enough to detect the weak luminescence from the tunnel junction. This requires an intensified Peltier-cooled charge-coupled device (CCD) camera to image the luminescence light spot and to picture immediately afterwards the tip and its reflection under illumination by an external light and at reduced intensifier voltage. Figure 4(c) shows on overlay of such two images allowing for an identification of the exact position of the tip apex. Figure 4(b) shows a plot of the CCD raw data without pixel binning and a cross section (red line above) through the maximum. This image of the luminescence from tip-induced plasmons demonstrates that the chosen aspheric lens is sufficient to obtain a spot with the dimension of a few pixels even at visible wavelengths.

B. Angular distribution of light emission

The use of free propagating beams (in contrast to a glass fiber guided coupling) allows preserving a maximum of information carried by the light. One such source of information is the angular distribution of emitted light, which is only rarely monitored in STM-induced luminescence.[19] When the focus is purposely shifted away from the CCD plane, a broad spot is observed. This extended distribution represents the 2D Fourier transform of the waves composing the image of the light emitting point. It can be immediately interpreted as the angular distribution of the light emitted from the tip-sample region. The principle is illustrated in Fig. 4(a) by the dashed and the dotted beam propagating at some angle with respect to the optical axis. Figure 4(d) shows the angular distribution obtained in the Fourier-transforming geometry in one of the light paths. Our example maps the anisotropy found in the emission from tip-induced surface plasmons on a metallic sample. We discuss the color-coding in this figure in Sec. III C. The deviation from the circular shape demonstrates that the anisotropy of light emission in the azimuthal direction is less pronounced than the anisotropy for varying elevation angle. The tip-sample orientation in Fig. 4(d) is the same as in Fig. 4(c). The measurable azimuthal emission distribution can in principle be extended further by including the information from the other two ports. We observed that the intensity from tip-induced plasmons in the three light paths can vary significantly. As the three paths are almost identical by design, we ascribe this observation to the irregularity of the tip apex and the resulting differences in the coupling of tip-induced plasmons to the emitted far field.[21] We did not yet investigate angular information for light sources other than tip-induced plasmons. However, we suggest that the observation of angular luminescence distributions can contribute to the characterization of anisotropic emitters such as, e.g., quantum wires or luminescent molecules. The identification of nodes in the angular distribution allows an assignment of the orientation of the local transition dipole that has been introduced by far-field microscopy studies of single molecules.[22,23]

C. Polarization analysis of luminescence

The information obtained by the angular distribution of luminescence can be supplemented by polarization analysis. Figure 5(a) shows a polar plot of the integrated light intensity from one lens as a function of polarizer angle. The data (red dots) were fitted (blue line) by a sum of two components, an isotropic one (green curve) and a dipolar one (red curve). The result clearly indicates a dominant direction of

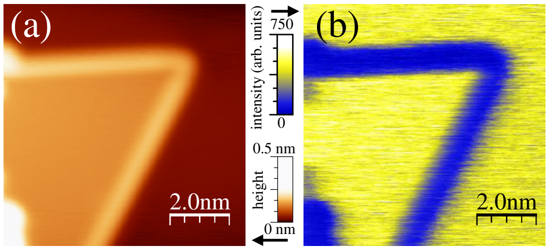

FIG. 6. (Color online) (a) Topographic scan with a simultaneous acquisition of (b) luminescence intensity. Ag coated W tip on Ag(111), bias U=3.0 V, tunnel current I=0.5 nA, 512×512 data points, and scanning speed of 1.8 s per line. Bandwidth of luminescence channel 10 Hz. The plots were made using WSXM (Ref. 31) software.

the electric field vector in the radiation. As the direction of observation is not identical to the one in Figs. 4(c) and 4(d) the apparent orientation of the surface normal is different. We employ a realistic visual simulation of the 3D geometry [software: POV-RAY (TM) for WINDOWS, version 3.5] that reproduces realistically the actual view into one of the viewports. The simulated view toward the aspheric lens [Fig. 5(b)] allows determining the projection angle of the coordinates in the STM and proves that the preferential polarization of the tip-induced plasmons is parallel to the surface normal (p-polarization). This may appear obvious when regarding the electric field associated with the tip-induced plasmon. It might be more surprising that the component polarized parallel to the surface (s-polarization) is comparable in intensity to the p-polarized contribution (red curve). The use of a quarter wave plate can in addition determine the circularly polarized component. A full polarization analysis has been discussed by Pierce *et al.*[24] The spectra in the direction of maximum intensity (blue) and minimum intensity (green) are plotted in Fig. 5(c) together with the difference of the two spectra (red) with the color coding equivalent to the polar plot in Fig. 5(a). The two linear polarization components show no significant spectral difference. Finally, we demonstrate the measurement of the polarization-resolved angular distribution by combining Fourier imaging (see Sec. III B) with polarization analysis. Figure 4(d) is a color coded overlay of the polarized contribution and the s-polarized contribution (blue and yellow, respectively). It is remarkable that the s-polarized contribution varies strongly with the azimuth of emission. This supports the assignment to tip apex irregularities suggested in Sec. III B.

D. Spatial luminescence mapping and tunneling excitation spectroscopy

Figure 6 demonstrates the ability to record a map of the total emitted light intensity in STM scanning mode. The luminescence image was recorded during a detailed 30 min topography scan (512×512 pixel, current 0.5 nA). The short charge pulses (<1 μs) from the single channel detector, here a photomultiplier tube (PMT), were integrated by a commercial measuring amplifier (DC-1000, Alexander Meier Elektronik, Germany) with the bandwidth reduced to 10 Hz. This low pass filtered signal is then fed to a separate input channel of the STM scanning electronics. The observed reduction of luminescence intensity near step edges with respect to terraces has been discussed earlier.[25,26] In our measurement, it can be related to an increased tip-sample distance shown by the bright edges in the topographic image. The tip retraction is not a dynamic effect from the STMs feedback loop at the step-edge because the same behavior is observed for step edges parallel and perpendicular to the scanning direction. It can be due to a reduced tunnel barrier or an increased density of states.

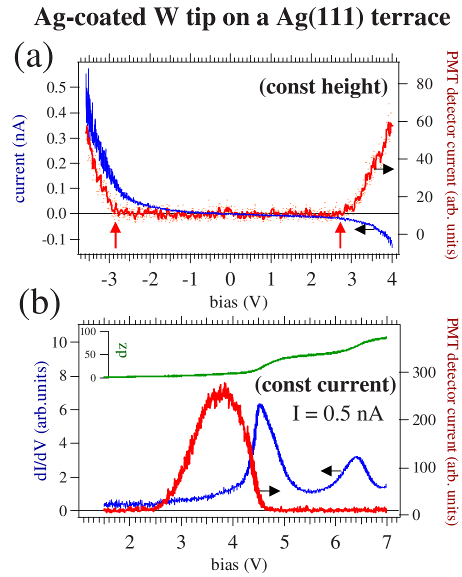

FIG. 7. (Color online) Tunneling spectroscopy (I and dI/dV: scales on the left-hand side) with simultaneous recording of total luminescence intensity using a PMT (scales on the right-hand side) for a Ag coated W tip on Ag(111). Single forward and backward bias scan at 10 s per sweep. Bandwidth of luminescence channel 10 Hz. (a) Constant height mode, set point V=−3.6 V, I=0.5 nA. (b) Constant current mode, I=0.5 nA. Top trace in (b): height change of the STM tip during bias sweep.

In the same way as in topographic scans, one can record a bias-dependent luminescence synchronously with the acquisition of tunnel current and differential resistance (dI/dV data from a lock-in amplifier). Figure 7 shows examples for a single forward and backward bias sweep acquired within 20 s. Recording this type of excitation spectrum at constant height condition [Fig. 7(a)] yields the light emission onset at both polarities, here at similar absolute voltages (arrows pointing up). This is due to the fact that with a few exceptions,[27,28] a photon is not found to carry more energy than provided by a single tunneling charge. The photon generation efficiency can be obtained by dividing the light intensity by the current [represented by the two traces in Fig. 7(a)]. This ratio can be obtained directly, and with higher precision, in a constant current measurement as in Fig. 7(b). The decrease of the quantum efficiency above 4 V may in part be due to the retraction of the tip from the surface (green curve) that occurs in response to an increased conductance due to the upcoming first field ionization resonance at 4.5 V. As the tip-induced light emission requires the proximity of tip and surface a tip retraction leads to a reduction of the light emission.[29]

E. Chromatic aberration in luminescence spectra

An important type of measurement that contains rich information on the studied photon source is the light spectros-

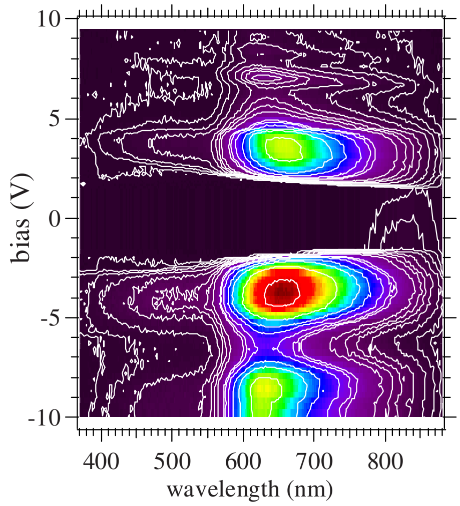

FIG. 8. (Color online) "Fingerprint" measurement of tip-induced plasmon polaritons for a W tip on an atomically flat terrace on Cu(110). The 76 separate spectra recorded with a tunnel current I=1 nA for different bias voltage (y-scale) are presented in a 2D intensity plot together with white contour lines of equal intensity (the intensities for which the contour lines are drawn are arbitrarily chosen).

copy at a previously characterized surface position. We present as an example spectra recorded with a W tip on a terrace of a Cu(110) single crystal. In Fig. 8, the light intensity is plotted in a reverse rainbow color scale as a function of bias voltage (y-axis) and wavelength (x-axis). This plot is overlaid with contour lines of constant light intensity. The plot is composed of single plasmon spectra with a total accumulation time of 2.7 h and provides an overview of the relation between excitation energy (bias voltage) and emission energy (plasmon wavelength). We note that for the constant current condition the bias voltage is connected with the tip-sample distance in a monotonic but not linear relation.

A prerequisite of detailed spectroscopic data is a high resolution of the imaging optics. In order to reduce losses, we operate the spectrometer with a wide entrance slit. Figure 9 shows a false color (reverse rainbow) representation of the pixelwise readout from the CCD chip at the spectrograph. Such data is the basis for the generation of spectra. The broad spectral distribution of tip-induced plasmon emission in this example allows the visualization of a bow-tie shaped pattern in Fig. 9. The focus obtained at the center is comparable to the diameter of the radiation source image in Fig. 4(b). The broadening toward the sides of the spectrum can be attributed to the chromaticity of the aspheric lens in our setup as well as astigmatism and other aberrations of the spectrometer. Changing the focus in the spectrometer allows shifting the center of the bow-tie to higher or lower wavelengths. Conventionally integrated spectra obtained from the CCD array thus achieve the instruments limiting spectral resolution only over a restricted wavelength range. If a larger range has to be covered, the spectra have to be measured for every wavelength interval at a different focal setting of the imaging lens outside the UHV chamber. Alternatively, the data from the CCD array can be deconvoluted by a wavelength-dependent broadening.

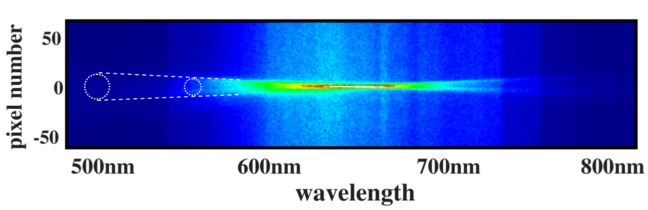

FIG. 9. (Color online) Spectroscopic CCD raw data (1024×256 pixels) characterizing the chromatic aberration of the optical system (see text).

IV. OUTLOOK

Other types of measurements can be performed with the presented setup but are beyond the scope of this paper. New opportunities are opened by simultaneous use of the three optical ports: First, light can be coupled into the tunnel junction through one port allowing for photoluminescence measurements either with the STM tip removed or in place. Focal spots down to 3 μm may be achievable. The field enhancement in the presence of the metallic tip will increase the spatial confinement of incoming light to dimensions near the curvature of the tip apex (10–50 nm) similar as in apertureless near-field optical microscopes.[32,33] Second, one can imagine equipping two optical ports each with a time-resolving photon detector. Fast processes induced by the STM tunnel current can thus become accessible via time-correlation techniques. We presently explore this combination of ns time resolution with the subnanometer spatial resolution of the STM.

ACKNOWLEDGMENTS

We thank Oguzhan Gürlü for the valuable advice to improve the performance of the scanning tunneling microscope and his help during the assembly.

[1] J. K. Gimzewski, B. Reihl, J. H. Coombs, and R. R. Schlittler, Z. Phys. B: Condens. Matter **72**, 497 (1988).
[2] R. Berndt, J. K. Gimzewski, and P. Johansson, Phys. Rev. Lett. **67**, 3796 (1991).
[3] L. Samuelson, A. Gustafsson, J. Lindahl, L. Montelius, M. E. Pistol, J. O. Malm, G. Vermeire, and P. Demeester, J. Vac. Sci. Technol. B **12**, 2521 (1994).
[4] X. H. Qiu, G. V. Nazin, and W. Ho, Science **299**, 542 (2003).
[5] Z. C. Dong, X. L. Guo, A. S. Trifonov, P. S. Dorozhkin, K. Miki, K. Kimura, S. Yokoyama, and S. Mashiko, Phys. Rev. Lett. **92**, 086801 (2004).
[6] E. Ćavar, M.-C. Blüm, M. Pivetta, F. Patthey, M. Chergui, and W.-D. Schneider, Phys. Rev. Lett. **95**, 196102 (2005).
[7] S. W. Wu, G. V. Nazin, and W. Ho, Phys. Rev. B **77**, 205430 (2008).
[8] S. F. Alvarado and P. Renaud, Phys. Rev. Lett. **68**, 1387 (1992).
[9] K. Perronet, G. Schull, P. Raimond, and F. Charra, Europhys. Lett. **74**, 313 (2006).
[10] N. Nilius, A. Cörper, G. Bozdech, N. Ernst, and H. J. Freund, Prog. Surf. Sci. **67**, 99 (2001).
[11] G. Hoffmann, J. Kroger, and R. Berndt, Rev. Sci. Instrum. **73**, 305 (2002).
[12] A. Barbara, T. Lopez-Rios, and P. Quemerais, Rev. Sci. Instrum. **76**, 023704 (2005).
[13] N. J. Watkins, J. P. Long, Z. H. Kafafi, and A. J. Makinen, Rev. Sci. Instrum. **78**, 053707 (2007).
[14] J. Steidtner and B. Pettinger, Rev. Sci. Instrum. **78**, 103104 (2007).
[15] D. Zhang, X. Wang, K. Braun, H.-J. Egelhaaf, M. Fleischer, L. Hennemann, H. Hintz, C. Stanciu, C. J. Brabec, D. P. Kern, and A. J. Meixner, J. Raman Spectrosc. **40**, 1371 (2009).
[16] R. Berndt, R. Gaisch, W. D. Schneider, J. K. Girazewski, B. Reihl, R. R. Schlittler, and M. Tschudy, Surf. Sci. **307–309**, 1033 (1994).
[17] M. Kemerink, J. W. Gerritsen, J. G. H. Hermsen, P. M. Koenraad, H. van Kempen, and J. H. Wolter, Rev. Sci. Instrum. **72**, 132 (2001).

[18] T. Murashita, J. Vac. Sci. Technol. B **15**, 32 (1997).
[19] R. Berndt, R. R. Schlittler, and J. K. Gimzewski, J. Vac. Sci. Technol. B **9**, 573 (1991).
[20] M. Vogelgesang, Ph.D. thesis, Ecole Politechnique Fédérale de Lausanne, 2005.
[21] T. Kalkbrenner, U. Hakanson, and V. Sandoghdar, Nano Lett. **4**, 2309 (2004).
[22] E. Betzig and R. J. Chichester, Science **262**, 1422 (1993).
[23] J. Jasny and J. Sepiol, Chem. Phys. Lett. **273**, 439 (1997).
[24] D. T. Pierce, A. Davies, J. A. Stroscio, and R. J. Celotta, Appl. Phys. A: Mater. Sci. Process. **66**, S403 (1998).
[25] R. Berndt and J. K. Gimzewski, Phys. Rev. B **48**, 4746 (1993).
[26] R. Branscheid, V. Jacobsen, and M. Kreiter, Surf. Sci. **602**, 176 (2008).
[27] G. Hoffmann, R. Berndt, and P. Johansson, Phys. Rev. Lett. **90**, 046803 (2003).
[28] Z. C. Dong, X. L. Zhang, H. Y. Gao, Y. Luo, C. Zhang, L. G. Chen, R. Zhang, X. Tao, Y. Zhang, J. L. Yang, and J. G. Hou, Nat. Photonics **4**, 50 (2010).
[29] R. Berndt and J. K. Gimzewski, Surf. Sci. **269–270**, 556 (1992).
[30] COCREATE (CoCreate Software, Inc., USA, 2006).
[31] I. Horcas, R. Fernandez, J. M. Gomez-Rodriguez, J. Colchero, J. Gomez-Herrero, and A. M. Baro, Rev. Sci. Instrum. **78**, 013705 (2007).
[32] R. Esteban, R. Vogelgesang, and K. Kern, Nanotechnology **178**, 475 (2006).
[33] A. Bek, R. Vogelgesang, and K. Kern, Rev. Sci. Instrum. **77**, 043703 (2006).